ARTICLE

Check for updates

Spin-texture-driven electrical transport in multi-Q antiferromagnets

Soonbeom Seo [1✉], Satoru Hayami [2], Ying Su[1], Sean M. Thomas [1], Filip Ronning[1], Eric D. Bauer [1], Joe D. Thompson[1], Shi-Zeng Lin [1] & Priscila F. S. Rosa [1✉]

Unusual magnetic textures can be stabilized in f-electron materials due to the interplay between competing magnetic interactions, complex Fermi surfaces, and crystalline anisotropy. Here we investigate $CeAuSb_2$, an f-electron incommensurate antiferromagnet hosting both single-Q and double-Q spin textures as a function of magnetic fields (H) applied along the c axis. Experimentally, we map out the field-temperature phase diagram via electrical resistivity and thermal expansion measurements. Supported by calculations of a Kondo lattice model, we attribute the puzzling magnetoresistance enhancement in the double-Q phase to the localization of the electronic wave functions caused by the incommensurate magnetic texture.

[1] Los Alamos National Laboratory, Los Alamos, NM, USA. [2] Department of Applied Physics, The University of Tokyo, Tokyo, Japan.
✉email: soondangs@gmail.com; pfsrosa@lanl.gov

f-based materials often exhibit complex magnetic ground states[1–3], which include spin helix[4], conical spiral[5], and more exotic spin textures with nontrivial topology, such as skyrmions[6–8]. Magnetic textures play a central role in understanding material's properties because of the coupling between spin, charge, and lattice degrees of freedom. For instance, spin textures may influence the electronic transport by partially gapping out states near the Fermi level, and incommensurate textures can cause localization of the electronic wave functions in the strong coupling regime[9–12]. Notably, spin textures can also produce a nonzero Berry curvature and Hall conductivity by breaking certain symmetries[13–16].

Magnetic cerium-based compounds are a particularly relevant platform to understand the role of spin textures because their magnetic ground states can be tuned by using modest nonthermal parameters, such as pressure and magnetic field. One example is tetragonal $CeAuSb_2$, in which a conventional single-Q ($1Q$) magnetic order, as well as a more exotic double-Q ($2Q$) magnetic order are stabilized as a function of magnetic fields (H) applied along the *c*-axis. In both phases, magnetic moments point along the *c*-axis due to the strong Ising spin anisotropy. At zero field, $CeAuSb_2$ orders antiferromagnetically below $T_N = 6.3$ K in a $1Q$ stripe structure with wave vector $\mathbf{Q}_1 = (\eta, \eta, 1/2)[\eta = 0.136 (2)]$[17–21]. A $2Q$ phase emerges in the region between $H_{c1} = 2.8$ T and $H_{c2} = 5.6$ T before magnetic moments in $CeAuSb_2$ becomes fully polarized. A tricritical point of H_{c2} has been previously identified and signals the change in the field-induced transition from second to first order, as temperature is decreased[19].

Notably, the stripe pattern with twofold rotational symmetry in the *ab*-plane has been recently shown to be associated with a nematic state—an electronic state that breaks the rotational symmetry of the underlying lattice, but not its translational symmetry[22]. This nematic state, which sets in just above T_N, is accompanied by a structural transition that is strongly coupled to the $1Q$ stripe phase below H_{c1} (ref. [22]). Whether this nematic state survives in the $2Q$ phase remains an open question, and whether the $2Q$ structure is checkerboard (C_4-symmetric) or woven (C_2-symmetric) remains a matter of contention[20,23].

Electrical transport data also pose intriguing questions. The electrical resistivity of $CeAuSb_2$ increases when the material transits from the $1Q$ state to the $2Q$ state[18,19]. In the fully polarized state, the resistivity drops to a value smaller than that in zero field. A recent explanation for the enhanced resistivity in the $2Q$ state relies on quasi-nesting of the itinerant Fermi surface[20]. Nonetheless, the field dependence of the resistivity in $CeAuSb_2$ remains poorly understood, and whether it is better described by a localized or itinerant $4f$-electron picture remains controversial[20,24].

To address these questions, we first map out the H–T phase diagram of $CeAuSb_2$ by means of high-resolution electrical resistivity and thermal expansion measurements (Fig. 1a). The presence of two nearby transitions as a function of temperature for fields between H_{c1} and H_{c2} suggests that the coupled structural–magnetic transition survives in the $2Q$ phase. Supported by calculations of a Kondo lattice model, we attribute the puzzling field dependence of the electrical resistivity (Fig. 1b) in different magnetic states to the localization of electronic wave functions due to the spin textures. Importantly, our analysis reveals that it is not possible to simultaneously nest two pairs of hot spots by the $2Q$ state. We therefore propose that the field-dependent electronic transport of $CeAuSb_2$ acts as a fingerprint of the different spin textures.

Results

Thermal expansion and electrical resistivity. First, we determine the H–T phase diagram of $CeAuSb_2$ by thermal expansion and
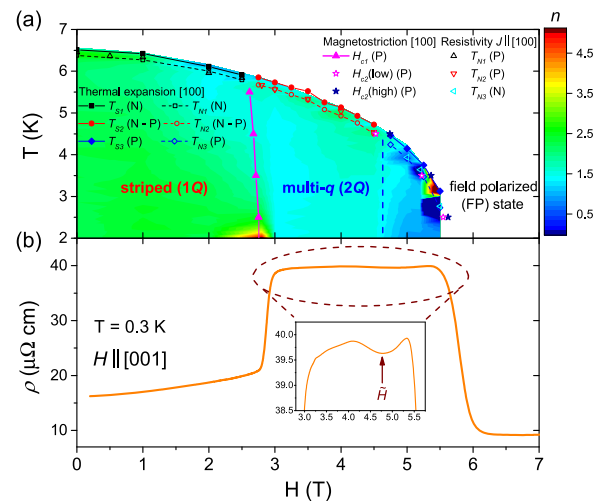

Fig. 1 Phase diagram of $CeAuSb_2$ its unusual magnetoresistance. a Temperature–magnetic field phase diagram of $CeAuSb_2$. The legend identifies how transition temperatures and fields are obtained. The solid squares, circles, and diamonds indicate the higher transition temperature T_s in three regions. The open squares, circles, and diamonds indicate the lower transition temperature T_N in three regions. The solid triangles indicate the first critical field H_{c1} separating single-q and multi-q phases. The open and solid stars indicate the lower and higher second critical fields, respectively. The open up triangles, down triangles, and left triangles indicate T_N in three regions. The sign of the peaks in the derivative are indicated in brackets: N negative, P positive. Colors represent the local exponent, $n = \partial\ln\Delta\rho/\partial\ln T$ and $\Delta\rho = \rho_{ab} - \rho_0 = AT^n$. The contour map shows the presence of three distinct regions in the phase diagram; the green, light-blue, and deep-blue regions denote the single-Q stripe phase ($1Q$), multi-Q phase ($2Q$) below $\tilde{H}$, and multi-Q phase ($2Q$) above $\tilde{H}$. Dashed vertical line inside $2Q$ phase denotes a crossover boundary at $\tilde{H}$. **b** Electrical resistivity as a function of applied field along the *c*-axis. The inset shows an anomaly at the crossover field $\tilde{H}$. Error bars are smaller than the size of the data points.

electrical resistivity measurements. The results are compiled in Fig. 1a. The overall structure of the phase diagram agrees with previous results; however, our thermal expansion measurements reveal an additional phase transition that has been overlooked[19,21,23]. Figure 2a shows the temperature dependence of the thermal expansion, $\Delta L/L$, of $CeAuSb_2$ along [001] at various magnetic fields applied parallel to the *c*-axis. The anomalies in $\Delta L/L$ in the vicinity of T_N are qualitatively different from the typical anomaly expected for a single magnetic phase transition. In fact, two peaks are observed in the linear thermal expansion coefficient, $\alpha = (1/L)(dL/dT)$, along [001] (Fig. 2b) and [100] (Supplementary Fig. 1b). Recent X-ray diffraction data point to the presence of a structural transition nearly coincident with the zero-field T_N, which suggests that the presence of two phase transitions in thermal expansion is a signature of the coupled structural–magnetic phase transition[22]. Therefore, our thermal expansion measurements reveal that structural and magnetic transitions remain strongly coupled in $2Q$ phase, as two phase transitions are also detectable above H_{c1}.

Figure 2b shows the temperature dependence of the longitudinal linear thermal expansion coefficient when fields of 1 and 5 T are applied along the *c*-axis. A small amount of uniaxial *c*-axis pressure was applied to the sample when mounting it in a capacitance dilatometer. The estimated stress is 0.07 and 0.02 GPa for high- and low-strain conditions, respectively. Under high strain, the amplitude of the largest peak in α_c is reduced by 16% at 1 T and 7% at 5 T compared to the low-strain data, whereas the amplitude of smallest peaks are remarkably suppressed by 66% at
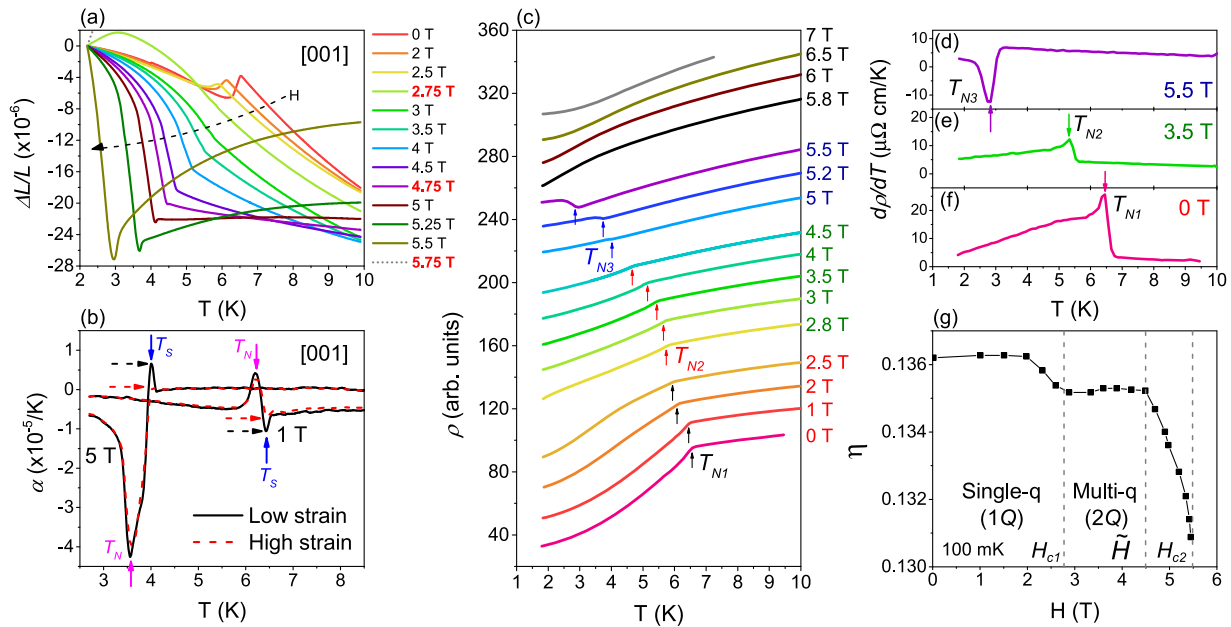
Fig. 2 Field evolution of phase transitions and ordering wave vector in CeAuSb₂. a Temperature dependence of the thermal expansion of CeAuSb$_2$ along [001] at various magnetic fields applied along the c-axis. Labels in bold indicate H_{c1}, $\tilde{H}$, and H_{c2}. **b** Temperature dependence of the linear thermal expansion coefficient along [001] with 1 and 5 T applied along the c-axis. The estimated pressure is 0.07 and 0.02 GPa for high-(dashed line) and low-(solid line) strain measurements, respectively. Solid arrows indicate peak positions: blue and magenta arrows for the T_s and T_N, respectively. Dashed arrows indicate points of minor peaks under low and high strains. **c** Temperature dependence of the in-plane electrical resistivity, ρ_{ab}, of CeAuSb$_2$ for applied magnetic fields along c-axis. Data at different fields are shifted for clarity. Arrows indicate antiferromagnetic transition temperatures: black, red, and blue arrows for the T_{N1}, T_{N2}, and T_{N3}, respectively. **d–f** Temperature derivative of ρ_{ab} under applied fields as a function of temperature at 5.5 T (**d**), 3.5 T (**e**), and 0 T (**f**). **g** Magnetic ordering wave vector $\eta[r, l, u.]$ for $\mathbf{Q}_1 = (\eta, \eta, 1/2)$ in CeAuSb$_2$ as a function of magnetic field applied along the c-axis at 100 mK. Data from ref. [20] were obtained by neutron diffraction measurement. Dashed lines at H_{c1}, $\tilde{H}$, and H_{c2} separate three distinct regions. Error bars are smaller than the size of the data points.

1 T and 89% at 5 T. Though the field-dependent magnetic phases are different and the sign of the two peaks are reversed between 1 and 5 T, the smaller peaks at higher temperature are always more sensitive to [001] strain than the largest peaks at lower temperature. Therefore, these results indicate that in CeAuSb$_2$ (i) the higher transition temperature at T_s is consistent with a structural transition, as structural transitions are naively expected to be more sensitive to lattice distortions caused by uniaxial strain than magnetic transitions, and (ii) the coupled phase transitions are preserved at high field, namely the zero-field coupled structural–magnetic transition survives in the 2Q phase. Lastly, the thermal expansion signatures of the phase transitions in CeAuSb$_2$ dramatically change not only at H_{c1} and H_{c2}, but also at 4.75 T, suggesting a new field boundary at $\tilde{H} = 4.75$ T (see Fig. 2a and Supplementary Fig. 1a).

Next, we turn to the field dependence of the electrical transport in CeAuSb$_2$. Figure 2c shows the temperature dependence of the in-plane resistivity, ρ_{ab}, under various magnetic fields applied along the c-axis. At low fields, a sharp drop at T_{N1} (black arrows) marks the magnetic transition temperature to a 1Q stripe phase. T_{N1} decreases with increasing field, and above H_{c1} a shallower kink-like anomaly (red arrows) occurs at T_{N2}, which is the magnetic transition temperature to a 2Q phase. As the field is further increased, T_{N2} decreases, and the temperature dependence of ρ_{ab} below T_{N2} remains virtually unchanged to 4.5 T.

Above 4.5 T, however, the signature of the magnetic transition, indicated by blue arrows at T_{N3}, changes qualitatively. Previous reports have missed this crossover field likely because its signatures occur in a very narrow field region. Above $\tilde{H} \approx 4.75$ T, ρ_{ab} increases on cooling through T_{N3}, which indicates the opening of a gap. As T_{N3} is suppressed toward zero temperature

with field, the magnitude of the jump increases. Finally, there is no evidence for a phase transition above $H_{c2} = 5.6$ T.

Figure 2d–f shows the derivative of the electrical resistivity, $d\rho/dT$, as a function of temperature at 0, 3.5, and 5.5 T. A large positive peak in $d\rho/dT$ is observed at T_{N1}, whereas a small positive peak is observed at T_{N2} and 3.5 T. At 5.5 T, however, a sharp negative peak is observed at T_{N3}, indicating that the behavior of $d\rho/dT$ crosses over at $\tilde{H}$. Even though a detectable upturn is observed at $\tilde{H}$ in the magnetoresistance of CeAuSb$_2$ at low temperature (inset of Fig. 1b), the absence of an anomaly at $\tilde{H}$ in the Hall resistivity[25] and magnetostriction, which is a thermodynamic probe, suggests the presence of a crossover at $\tilde{H}$ rather than a phase transition (see Supplementary Note 1). The contour map of the local exponent n of ρ_{ab} shows a change in magnetic scattering below T_N in the vicinity of $\tilde{H}$ (Fig. 1a), in agreement with a crossover field boundary at $\tilde{H}$ in the 2Q phase. Previous reports have been overlooked the crossover behavior in 2Q phase due to a narrow field range between $\tilde{H}$ and H_{c2} (~0.7 T). In fact, the color map of the exponent n in ref. [22] does not display the signature of crossover in $\rho(T)$ above $\tilde{H}$ because of the lack of the data in the vicinity of H_{c2}. Nonetheless, the tricritical point of H_{c2} has been previously located near $\tilde{H}$ and 4 K, which strongly suggests that $\tilde{H}$ coincides with the tricritical point of H_{c2}. As a result, $\tilde{H}$ not only represents a crossover as a function of magnetic fields at fixed temperature, but it also marks a change in the nature of the magnetic phase transition as a function of temperature at fixed fields. For fixed fields below $\tilde{H}$, the antiferromagnetic phase transition at T_N is of the second order, whereas the transition becomes first order at T_N (i.e., hysteretic) when $H > \tilde{H}$ (ref. [19]). We note that the tricritical point of H_{c2} does

not change under pressure[22]. Importantly, the wave vector component η decreases as a function of field when $H > \tilde{H}$ as shown in Fig. 2g (ref. [20]). As discussed below, the upturn of resistivity for $H > \tilde{H}$ stems from the intertwined effects of a varying ordering wave vector and the electronic localization of wave functions.

Spin Hamiltonian. After determining the experimental H–T phase diagram of CeAuSb$_2$, we now provide a theoretical model to understand it. In CeAuSb$_2$, Ce^{3+} ions carry a magnetic moment and interact with the conduction electrons, which in turn mediate interaction between cerium moments. Therefore, a sensible starting point to describe the magnetic properties of CeAuSb$_2$ is the Ruderman–Kittel–Kasuya–Yosida (RKKY) interaction. In the paramagnetic phase, the system has C_4 rotation symmetry, and the appearance of a $1Q$ magnetic state implies that the Fermi surface is quasi-nested with nesting wave vectors $\mathbf{Q}_1$ and $\mathbf{Q}_2$, which are related by C_4 rotation. To second order in the local exchange coupling between the conduction electrons and localized moments, the Hamiltonian of the system reads $-\sum_Q \tilde{J}(Q)\mathbf{S}_Q \cdot \mathbf{S}_Q$, in which we have assumed an isotropic exchange coupling ($\tilde{J}$) among spins. Here $\mathbf{S}_Q$ is the Fourier component of the localized moment. The functional form of $\tilde{J}(Q)$ depends on the Fermi surface and in principle can be obtained from density functional calculations. The ground state magnetic texture implies that $\tilde{J}(Q)$ is maximized at $\mathbf{Q}_1$ and $\mathbf{Q}_2$. From experiments, a strong easy-axis anisotropy is also known to exist, which forces the spins to point along the c axis. In the presence of an external magnetic field, the system Hamiltonian can thus be written as:

$$\mathcal{H} = -\sum_Q \tilde{J}(Q)\mathbf{S}_Q \cdot \mathbf{S}_Q - A\sum_i S_{i,z}^2 - \sum_i \mathbf{H} \cdot \mathbf{S}_i. \quad (1)$$

In triangular lattices, $\mathcal{H}$ is known to support triple-Q spin textures (e.g., skyrmion lattice)[26–29]; however, in tetragonal crystals such as CeAuSb$_2$, $2Q$ order is not favored by $\mathcal{H}$ because the harmonic $\mathbf{Q}_3 = \mathbf{Q}_1 + \mathbf{Q}_2$ is not an optimal wave vector and costs energy. As an example, our Monte Carlo simulation of a particular form of $\tilde{J}(Q)$ within the frustrated J_1-J_2 or J_1-J_3 model on a square lattice shows a $1Q$ spiral phase followed by a fully polarized state in field[29].

In cerium-based compounds, the exchange interaction between $4f$ and conduction electrons is often substantial. In the strong coupling regime, the system becomes nonmagnetic due to Kondo singlet formation. In the weak coupling regime, the system becomes magnetic and the dominant exchange coupling is the conventional RKKY interaction. Importantly, even in this weak coupling regime, higher-order spin exchange interactions beyond the conventional RKKY interaction can be important[30]. By expanding the spin–charge coupling to quartic order, a four-spin interaction term emerges, which was demonstrated to favor multiple-Q magnetic ordering[31].

The existence of the $2Q$ order in CeAuSb$_2$ thus requires higher-order coupling, and the spin Hamiltonian is written as:

$$\mathcal{H} = 2\sum_\nu \left[-\tilde{J}\mathbf{S}_{\mathbf{Q}_\nu} \cdot \mathbf{S}_{-\mathbf{Q}_\nu} + \tilde{K}(\mathbf{S}_{\mathbf{Q}_\nu} \cdot \mathbf{S}_{-\mathbf{Q}_\nu})^2 \right] - A\sum_i S_{i,z}^2 - \sum_i \mathbf{H} \cdot \mathbf{S}_i. \quad (2)$$

In this model, $\tilde{J}(Q)$ is assumed to peak sharply at $\mathbf{Q}_\nu$, and therefore only the exchange coupling at $\mathbf{Q}_\nu$ is taken into account. Because the biquadratic interaction $K = N\tilde{K}$ (N is the system size) is always positive, the four-spin term favors multiple-Q ordering by distributing the static spin structure factor weight equally on the symmetry related $\mathbf{Q}_\nu$. In CeAuSb$_2$, spins along the

c-axis are simply antiferromagnetically coupled. Therefore, we will restrict to the two dimensional limit in the following discussions.

Figure 3 shows the numerical results of (a) the uniform magnetization $M = (1/N)\sum_i S_i^z$ and (b) the $\mathbf{Q}_\eta$-component magnetization $M_{\mathbf{Q}_\eta} = (1/N)\sqrt{|\sum_i S_i^z e^{i\mathbf{Q}_\eta \cdot \mathbf{r}_i}|^2}$ as a function of an external field. The field-dependent real-space spin configurations are shown in Fig. 3c–e, and their corresponding spin structure factors are shown in Fig. 3f–h. The optimal spin configuration at zero field is a $1Q$ collinear state whose spin configuration and spin structure factor are shown in Fig. 3c, f. Three magnetization jumps are identified by increasing field in Fig. 3a. The first jump at $H \sim 0.46$ represents a crossover from the up-up-up-down-down-down configuration in Fig. 3c to the up-up-up-up-down-down configuration in Fig. 3d, g, which results from the approximation of a sharply peaked $\tilde{J}(Q)$. This jump disappears for a smooth function of $\tilde{J}(Q)$, in agreement with experiments. The other two jumps in magnetization represent phase transitions from the $1Q$ collinear to the $2Q$ bubble state and from the $2Q$ bubble to the fully field polarized (FP) state, which are caused by the interplay between the multiple-spin interaction (K) and the easy-axis single-ion anisotropy (A). The spin configuration of the $2Q$ state is characterized by the collinear bubble structure without an xy spin component, as shown in Figs. 3e, h. The equivalent four peaks in the spin structure in Fig. 3h also indicate the formation a square bubble crystal. Note that the $2Q$ bubble state vanishes by taking $K = 0$ or $A = 0$.

By including temperature, we obtain a magnetic phase diagram consistent with experiments. It is important to note that the antiferromagnetic transition at zero magnetic field is second order, whereas the transition at H_{c2} at $T = 0$ is strongly first order[19]. At finite temperatures, we therefore generically expect a tricritical point of H_{c2} at which the nature of the phase transition at T_N changes from second to first order, as reported previously[19].

Theory: transport. In this section, we show that the resistivity enhancement in the $2Q$ phase can be fully modeled theoretically. Our model is based on two elements: (1) relatively strong coupling between localized moments and conduction electrons, and (2) incommensurate spin texture with respect to the atomic lattice.

The presence of an incommensurate magnetic texture is known to result in band folding. More specifically, an ordering wave vector $\mathbf{Q} = (p/q, 0, 0)$, wherein q and p are coprime integers, causes band folding q times, resulting in a smaller Brillouin zone. To illustrate the band folding mechanism, the inset of Fig. 4 displays the simplest example of a commensurate wave vector that folds the bands once (i.e., $q = 2$). The presence of exchange coupling may open a gap at the Brillouin zone boundary causing an increase in resistivity known as the superzone mechanism[32–34].

Incommensurate magnetic textures may have more profound effects on the electronic transport. Rigorously speaking, the band structure picture is no longer a good description of the electronic state because of the lack of translational invariance. The incommensurate potential induced by the magnetic texture to a certain extent works as random disorder, but with a weaker effect. Importantly, random disorder causes Anderson localization when the disorder potential is strong enough[9,11,12]. In the Anderson localized phase, in which the electronic wave functions are strongly localized in space, the system behaves as an insulator even though there exists a finite electronic density of states (DOS) at the Fermi energy. An intertwined insight into this problem comes from the realization that the incommensurate potential
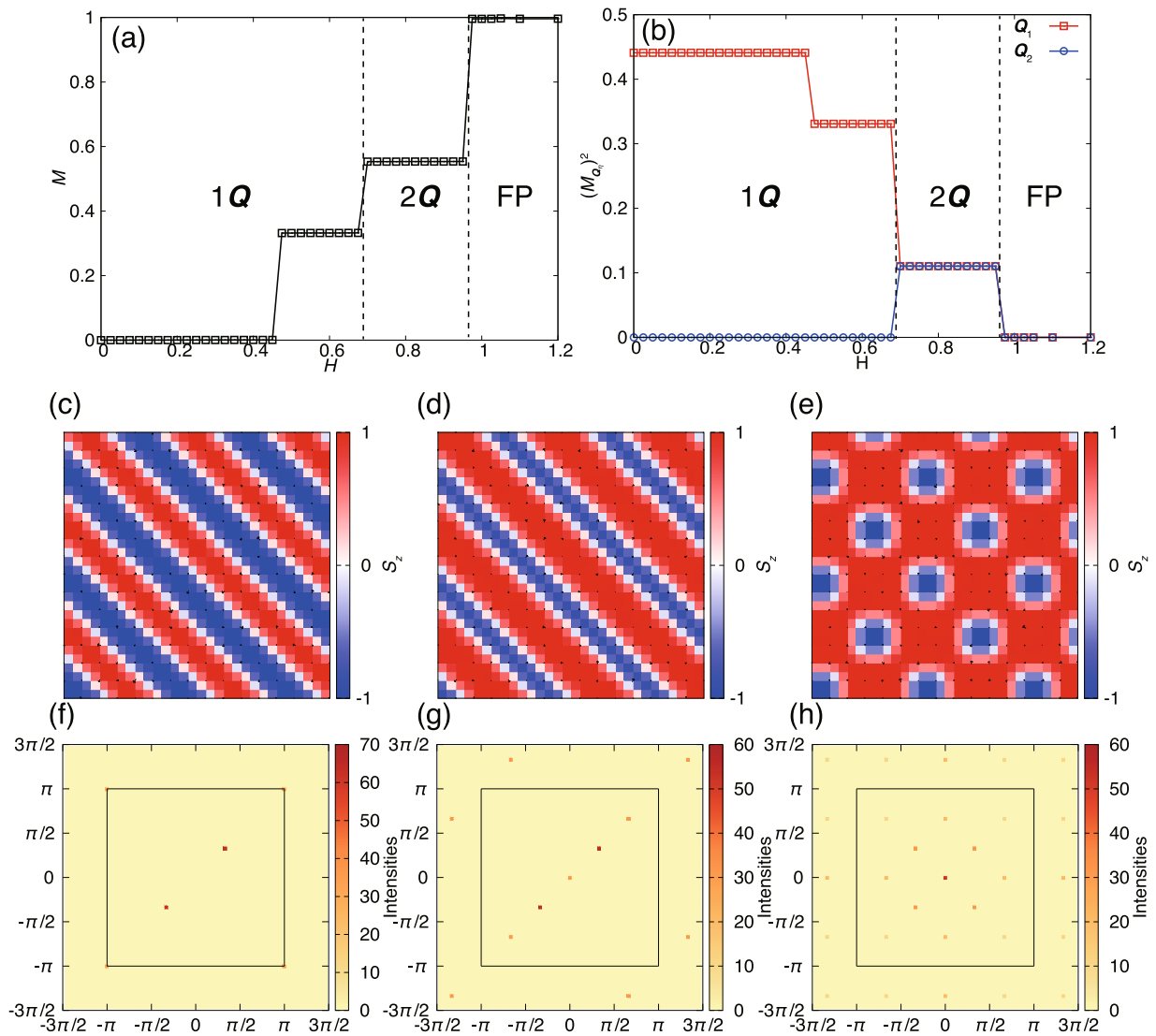
Fig. 3 Magnetization and spin configurations of CeAuSb₂. H dependences of the magnetization for **a** uniform component, and **b** $\mathbf{Q}_1$ (squares) and $\mathbf{Q}_2$ (circles) components at $\bar{J} = 1$, $K = 0.4$, and $A = 0.7$. The vertical dashed lines show the phase boundaries. **c–e** The real-space spin configurations in **c** the 1Q collinear state at $H = 0$, **d** the 1Q collinear state at $H = 0.6$, and **e** the 2Q bubble state at $H = 0.8$. The contour shows the z-component of the spin moment. **f–h** The square root of the spin structure factor. The solid squares represent the Brillouin zone.

can also cause electronic localization. This type of electronic localization was demonstrated in the Kondo lattice model hosting an incommensurate magnetic texture[12], and can be understood in terms of the band folding picture. Any incommensurate wave vector can be approximated by a rational number $Q \approx p/q$ with p, $q \to \infty$. The folded bands can be extremely flat in the folded Brillouin zone when levels repel each other due to the local exchange coupling. The flat band limit therefore corresponds to the electronic localization.

More specifically, we consider the following Kondo lattice Hamiltonian to model the electronic transport in CeAuSb₂:

$$\mathcal{H}_0 = -t_1 \sum_{\text{NN}} c_i^\dagger c_j - t_3 \sum_{\text{NNN}} c_i^\dagger c_j - \mu \sum_i c_i^\dagger c_i - J \sum_i c_{i,\alpha}^\dagger \sigma_{\alpha,\beta} \cdot \mathbf{S}_i c_{i,\beta}, \quad (3)$$

where NN and NNN denote nearest-neighbor and next-nearest-neighbor hopping, and J is the coupling between the conduction electron and spin texture. We choose the hopping strength $t_3 = -0.5t_1$ and chemical potential $\mu = 0.98t_1$, such that the Fermi surface is quasi-nested. The corresponding electronic filling per

spin is 0.638, which is fixed in the calculations. Equation (2) can be obtained from Eq. (3) by integrating out conduction electron degrees of freedom and expanding the exchange interaction to quartic order in J (ref. [31]). We choose experimentally measured incommensurate $Q = 0.136(2)$ and neglect the variation of Q under magnetic field. We fix the spin configurations in the calculations, and we take $\mathbf{S}_i = [0, 0, \cos(\mathbf{Q}_1 \cdot \mathbf{r}_i)]$ for the 1Q phase, $\mathbf{S}_i = [0, 0, \cos(\mathbf{Q}_1 \cdot \mathbf{r}_i) + \cos(\mathbf{Q}_2 \cdot \mathbf{r}_i)]/2$ for the 2Q phase, and $\mathbf{S}_i = [0, 0, 1]$ for the FP state.

The degree of localization of electronic wave functions can be characterized by the inverse participation ratio (IPR) defined as $I_n = \sum_{\mathbf{r}_i} |\psi_n(\mathbf{r}_i)|^4 (\sum_{\mathbf{r}_i} |\psi_n(\mathbf{r}_i)|^2)^{-2}$, where $\psi_n(\mathbf{r}_i)$ is the nth eigenfunction of $\mathcal{H}_0$. Because the IPR magnitude is a measure of the spread of the electronic wave function in space, higher IPR means a more localized state and hence smaller electrical conductivity. I_n is finite for a localized state but vanishes as $1/L^d$ for an extended state. Here L is the linear system size and d is the spatial dimension. The results of I_n and the profiles of the wave functions are displayed in Fig. 4. In the 1Q phase, the wave function along the $\mathbf{Q}$ direction is localized for large J, but remains extended
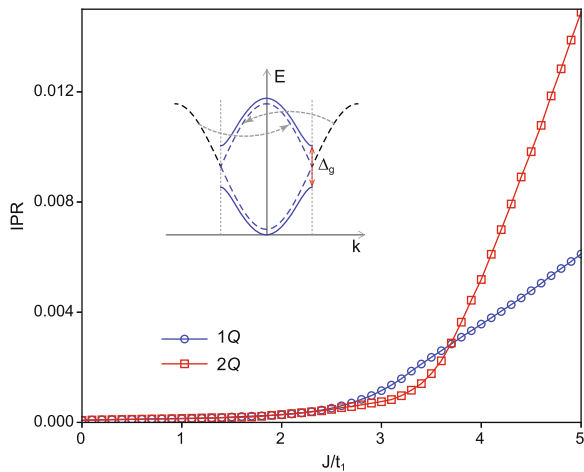
Fig. 4 Inverse participation ratio of CeAuSb$_2$. Inverse participation ratio (IPR) averaged over all the eigenvalues at 1Q (circles) and 2Q (squares) states. Error bars are smaller than the size of the data points. Inset illustrates the band folding and gap opening at the Brillouin zone boundary in the presence of a commensurate spin texture.
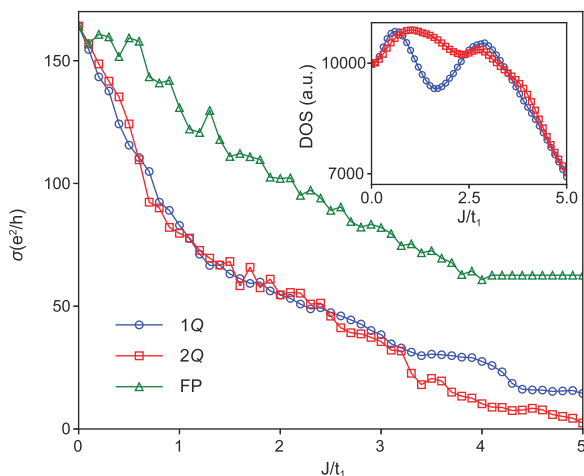

Fig. 5 Conductance vs J in different magnetic states and density of states of CeAuSb$_2$. J/t_1 dependence of the conductance for the 1Q (circles), 2Q (squares), and field polarized (FP) (triangles) states. Here, the conductance is averaged over domains with different Q orientations. Inset shows the density of state at the Fermi energy for the 1Q (circles) and 2Q (squares) states. Error bars are smaller than the size of the data points.

in the direction transverse to **Q** because of translational invariance. For the 2Q phase, the wave function is very localized at large J and becomes more localized than the 1Q counterpart for $J > 3.7t_1$.

Next, we calculate the electronic conductance under the influence of the magnetic texture. We focus only on the effect of the wave function localization by neglecting the scattering of electrons by impurities, magnetic fluctuations, and the off-diagonal conductivity caused by magnetic field. In fact, there is no sudden change in the off-diagonal resistivity when the spin texture changes from 1Q to 2Q in CeAuSb$_2$ (ref. [25]). As a result, the conductance depends on the DOS at the Fermi energy and the degree of the localization of the electronic wave function. The DOS for both 1Q and 2Q states, displayed in the inset of Fig. 5, indicates that the 2Q DOS is actually larger than the 1Q DOS for most Js, particularly for large J.

To compare our simulations to experiments, in which multiple domains of spin texture with different Q orientations coexist, we take the average of the longitudinal conductance over a random distribution of different Q domains (see Supplementary Note 3). Note that the dependence of the conductance remains qualitatively the same, if we assume that Q orientations are locked to the four equivalent crystal directions.

The conductance as a function J at $T = 0$ for three different spin textures is shown in Fig. 5. Overall, the conductance decreases with J due to electronic localization in the 1Q and 2Q phases. The decrease in the FP state is caused by the shift of the electronic spectrum due to the coupling to the FP spin arrangement, which results in the reduction of DOS at Fermi energy. Interestingly, in the region $J > 3.2t_1$, the conductance of the FP state is highest, followed by 1Q and 2Q states. This result is fully consistent with experimental observations in CeAuSb$_2$, namely, the resistivity in 2Q state is the largest and the resistivity in FP state is smallest (see Fig. 1b). Therefore, our theory model supports the notion that the incommensurate magnetic state is responsible for the increased resistivity in 2Q state. Though it is challenging to estimate J/t_1 without the experimental data or a microscopic model that can account for the strength of J in CeAuSb$_2$, our experimental and theoretical results suggest that CeAuSb$_2$ exhibits a large exchange coupling parameter between f and conduction electrons within the magnetically ordered regime.

Discussion

Enlightened by our model calculations, we are now positioned to understand the behavior of the electrical resistivity in CeAuSb$_2$. There are two competing effects at play: (1) the suppression of magnetic fluctuations when magnetic moments order below T_N, which reduces the resistivity, and (2) the enhancement of the degree of localization of 4f electronic wave function, which increases resistivity. The temperature- and field-dependent experiments in CeAuSb$_2$ indicate that the former factor is dominant in the 2Q phase above H_{c1}.

As recognized in ref. [20], spin textures might modify the resistivity by gapping out states near the Fermi level when the ordering wave vector corresponds to a nesting vector of the Fermi surface, i.e., the 1Q state would nest a pair of hot spots in the Fermi surface, whereas the 2Q state would nest two pairs. We note that this mechanism does not require the ordering wave vector to be incommensurate, and it also does not depend on whether the magnetic texture is of itinerant or localized origin.

The key result revealed by our analysis is that it is not possible to simultaneously nest two pairs of hot spots by the 2Q state. To exemplify this issue, let us consider four Fermi surface sheets $\epsilon(\mathbf{k}_1)$, $\epsilon(\mathbf{k}_2)$, $\epsilon(\mathbf{k}_1 + \mathbf{Q}_1)$, and $\epsilon(\mathbf{k}_2 + \mathbf{Q}_2)$, where $\mathbf{k}_1$ and $\mathbf{k}_2$ are related by C_4 rotation, and $\epsilon(\mathbf{k}_1)$ and $\epsilon(\mathbf{k}_1 + \mathbf{Q}_1)$ are quasi-nested by the vector $\mathbf{Q}_1$. For a 1Q collinear magnetic state with ordering wave vector $\mathbf{Q}_1$, the magnetic texture gaps out states in the Fermi sheets at $\epsilon(\mathbf{k}_1)$ and $\epsilon(\mathbf{k}_1 + \mathbf{Q}_1)$, and deforms the Fermi sheet at $\epsilon(\mathbf{k}_2)$ and $\epsilon(\mathbf{k}_2 + \mathbf{Q}_2)$. For the 2$Q$ state with $\mathbf{Q}_1$ and $\mathbf{Q}_2$ ordering wave vectors, the electronic states at $\epsilon(\mathbf{k}_1)$, $\epsilon(\mathbf{k}_1 + \mathbf{Q}_1)$, and $\epsilon(\mathbf{k}_1 + \mathbf{Q}_2)$ are mutually connected. However, this does not allow fully gapped states at $\epsilon(\mathbf{k}_1)$ and $\epsilon(\mathbf{k}_1 + \mathbf{Q}_1)$ as in the case of 1Q magnetic texture. Instead, the presence of 2Q only deforms the Fermi surface. We therefore reach the important conclusion that the electronic DOS within the 2Q phase is not necessarily smaller than that in the 1Q phase. This is demonstrated explicitly using the model in Eq. (3), in which the DOS for the 2Q phase is indeed comparable to that in the 1Q phase, as shown in Fig. 5. As a consequence, the enhanced resistivity in the 2Q phase is naturally explained by the enhanced localization of wave functions due to the incommensurate structure.

Further, an increase in the temperature-dependent resistivity at T_N is observed in experiments above $H > \tilde{H}$. We note that the magnetic transition at T_N becomes first order, magnetic fluctuations are not critical, and the ordering wave vector Q decreases continuously with applied magnetic fields. Importantly, a change in Q simultaneously affects the degree of localization of wave functions, the spin-dependent disorder potential, and band folding (e.g., the superzone mechanism), particularly when $Q < 2k_F$, wherein $2k_F$ is the Fermi momentum[35]. These intertwined factors therefore result in the observed upturn in $\rho(T)$ on cooling through T_N.

Finally, we turn to the discussion of the symmetry of the $2Q$ phase in CeAuSb$_2$. A neutron diffraction report showed that the $2Q$ magnetic order at high fields has two possible magnetic structures, i.e., checkered pattern with fourfold symmetry or woven pattern with twofold symmetry[20]. From their analysis, the authors conclude that the woven order might be favored because the field dependence of the maximum Ce^{3+} moment in this structure is consistent with the nature of the magnetization plateau of $M_{\mathbf{Q}_1+\mathbf{Q}_2}$ in the $2Q$ phase. From uniaxial strain measurements[23], however, it was proposed that the $2Q$ magnetic order most likely preserves the symmetry between the (100) and (010) directions, suggesting that the $2Q$ order is close to a checkerboard structure.

At zero field, a structural transition connected with $1Q$ magnetic order was recently discovered[22]. The H–T phase diagram and strain dependence of these coupled transitions suggest that the structural transition occurs above T_N and is coupled to the stripe magnetic order below H_{c1}. Here we observe that this coupling survives within the $2Q$ phase above H_{c1}, which indicates that a structural transition above T_N is still present and that the C_4 symmetry may be broken at the structural transition. Our results are therefore consistent with a woven structure or a deformed checkerboard. The effect of the structural transition can be modeled by using spatially anisotropic exchange coupling in the spin Hamiltonian (Eq. (2)), and it is expected to yield a distorted $2Q$ spin texture, e.g., by elongating the spin texture in Fig. 3e in the vertical direction, akin to the woven structure. Nevertheless, high-resolution spectroscopic measurements are required to unambiguously determine the magnetic structure of the $2Q$ phase. Here, we focus on c-axis strain because the structural and magnetic transitions exhibit opposite signs in thermal expansion along this direction. This enables the deconvolution of the phase transitions, in contrast to in-plane thermal expansion. In addition, to obtain meaningful information about in-plane nematicity, the applied in-plane strain must be sufficient to detwin the crystals, as shown for the case of K-doped BaFe$_2$As$_2$ (ref. [36]). Importantly, in the case of iron-based superconductors, crystals under [100] strain remain well twinned, which makes [110] strain necessary for detwinning them. We expect that [110] strain may be also required in the case of CeAuSb$_2$ because its magnetic order spontaneously lifts the (110)/(1$\bar{1}$0) degeneracy[37]. Our results will stimulate further measurements to investigate the nature of nematicity in both $1Q$ and $2Q$ phase, e.g., nematic susceptibility with in-plane [110] strain, similar to previous reports on iron-based superconductors[38].

Going beyond the electrical transport signatures investigated in the present work for CeAuSb$_2$, incommensurate multiple-Q spin textures are generally expected to significantly affect emergent quantum states. An incommensurate multiple-Q state breaks translation invariance, and it realizes a scenario similar to that of quasicrystals, in which a standard band structure theory based on crystal momentum is no longer applicable. Novel phenomena that do not have a counterpart in translationally invariant systems can thus appear[39,40]. Furthermore, the localization of electronic wave functions caused by incommensurate spin textures in the strong coupling regime can significantly enhance the Coulomb interaction or attractive interaction between electrons, which could lead to pronounced effects on many-body quantum states.

Here, we investigate CeAuSb$_2$, an f-electron incommensurate antiferromagnet, via electrical transport and thermal expansion measurements under applied fields along the c-axis. Our field–temperature phase diagram shows that the coupled structural–magnetic transition in the low-field $1Q$ phase survives in the high-field $2Q$. We also identify a crossover magnetic field, $\tilde{H} = 4.75$ T, above which the electrical resistivity increases upon cooling through the antiferromagnetic transition temperature. Our theoretical model demonstrates the electrical resistivity behavior of CeAuSb$_2$ in $1Q$, $2Q$, and fully polarized states. Supported by calculations of a Kondo lattice model, we attribute the resistivity enhancement in the $2Q$ phase to localization of the electronic wave functions caused by the incommensurate magnetic textures.

Methods

Crystal synthesis and experiments in magnetic fields. Single crystals of CeAuSb$_2$ were synthesized by a standard self-flux technique described in ref. [19] with Au excess to eliminate deficiency in the Au site. The orientation of the polished sample was verified by X-ray and Laue diffraction at room temperature. The thermal expansion and magnetostriction were measured using a capacitance cell dilatometer, as described by Schmiedeshoff et al.[41]. This design uses a CuBe spring to hold secure the sample. The spring constant was estimated using finite element analysis, which was used to calculate the uniaxial pressure applied to sample during measurement. A standard four-probe technique was employed to measure the in-plane electrical resistivity of CeAuSb$_2$, using a Model 372 AC Resistance Bridge. Two different cryostats were used to control temperature and magnetic field: a ^{4}He cryostat for measurement of temperature dependence of resistivity from 10 to 1.8 K and for applied magnetic fields along c-axis, and a ^{3}He cryostat for measurement of magnetoresistance at 0.3 K as a function of magnetic field applied along the c-axis to 7 T.

Monte Carlo simulation and quantum transport calculation. We perform Monte Carlo simulations for systems with $N = 96 \times 96$ spins by using standard approaches based on the Metropolis algorithm at target low temperatures. We numerically anneal the system to reach the ground state. The details of the simulation are discussed in Supplementary Note 2. To simulate quantum transport of the system, we consider a two-terminal setup. The details of the calculation are discussed in Supplementary Note 3.

Data availability

The data that support the findings of this study are available from the corresponding author upon request.

Code availability

Monte Carlo simulations were performed with a custom code using the standard Metropolis algorithm. All codes used for the analysis presented in this study are available from the corresponding author upon request.

References

1. Jensen, J. & Mackintosh, A. R. *Rare Earth Magnetism: Structures and Excitations* 1st edn. (Clarendon Press,1991).
2. Coleman, P. in *Handbook of Magnetism and Advanced Magnetic Materials*, 95–148 (Wiley, 2007).
3. Stewart, G. R. Heavy-fermion systems. *Rev. Mod. Phys.* **56**, 755–787 (1984).
4. Fobes, D. M. et al. Tunable emergent heterostructures in a prototypical correlated metal. *Nat. Phys.* **14**, 456–460 (2018).
5. Yakinthos, J., Semitelou, I. & Roudaut, E. Conical spiral in Tb$_5$Sb$_3$ compound. *Solid State Commun.* **59**, 227–231 (1986).
6. Kurumaji, T. et al. Skyrmion lattice with a giant topological Hall effect in a frustrated triangular-lattice magnet. *Science* **365**, 914–918 (2019).
7. Hirschberger, M. et al. Skyrmion phase and competing magnetic orders on a breathing kagomé lattice. *Nat. Commun.* **10**, 5831 (2019).
8. Khanh, N. D. et al. Nanometric square skyrmion lattice in a centrosymmetric tetragonal magnet. *Nat. Nanotechnol.* **15**, 444 (2020).

9.   Aubry, S. & André, G. Analyticity breaking and anderson localization in incommensurate lattices. *Ann. Israel Phys. Soc.* **3**, 18 (1980).

10. Hiramoto, H. & Kohmoto, M. Electronic spectral and wavefunction properties of one-dimensional quasiperiodic systems: a scaling approach. *Int. J. Mod. Phys. B* **06**, 281–320 (1992).

11. Devakul, T. & Huse, D. A. Anderson localization transitions with and without random potentials. *Phys. Rev. B* **96**, 214201 (2017).

12. Su, Y. & Lin, S. Z. Nontrivial topology and localization in the double exchange model with possible applications to perovskite manganites. *Phys. Rev. B* **98**, 235116 (2018).

13. Xiao, D., Chang, M.-C. & Niu, Q. Berry phase effects on electronic properties. *Rev. Mod. Phys.* **82**, 1959–2007 (2010).

14. Chen, H., Niu, Q. & MacDonald, A. H. Anomalous hall effect arising from noncollinear antiferromagnetism. *Phys. Rev. Lett.* **112**, 017205 (2014).

15. Nakatsuji, S., Kiyohara, N. & Higo, T. Large anomalous Hall effect in a non-collinear antiferromagnet at room temperature. *Nature* **527**, 212–215 (2015).

16. Asaba, T. et al. Large tunable anomalous hall effect in kagome antiferromagnet $U_3Ru_4Al_{12}$. *Phys. Rev. B* **102**, 035127 (2020).

17. Flandorfer, H. et al. On the cerium valence in ternary compounds $CeMSb_2$ and $CeM'Bi_2$; M = Mn,Fe,Co,Ni,Cu,Zn,Pd,Ag,Au and M' = Ni,Cu,Zn,Ag. *Solid State Commun.* **97**, 561–565 (1996).

18. Balicas, L. et al. Magnetic field-tuned quantum critical point in $CeAuSb_2$. *Phys. Rev. B* **72**, 064422 (2005).

19. Zhao, L. et al. Field-temperature phase diagram and entropy landscape of $CeAuSb_2$. *Phys. Rev. B* **93**, 195124 (2016).

20. Marcus, G. G. et al. Multi-q mesoscale magnetism in $CeAuSb_2$. *Phys. Rev. Lett.* **120**, 097201 (2018).

21. Seo, S. et al. Pressure effects on the heavy-fermion antiferromagnet $CeAuSb_2$. *Phys. Rev. B* **85**, 205145 (2012).

22. Seo, S. et al. Nematic state in $CeAuSb_2$. *Phys. Rev. X* **10**, 011035 (2020).

23. Park, J., Sakai, H., Mackenzie, A. P. & Hicks, C. W. Effect of uniaxial stress on the magnetic phases of $CeAuSb_2$. *Phys. Rev. B* **98**, 024426 (2018).

24. Thamizhavel, A. et al. Anisotropic electrical and magnetic properties of $CeTSb_2$ (T=Cu, Au, and Ni) single crystals. *Phys. Rev. B* **68**, 054427 (2003).

25. Lorenzer, K. A., Strydom, A. M., Thamizhavel, A. & Paschen, S. Temperature-field phase diagram of quantum critical $CeAuSb_2$. *Phys. Status Solidi B* **250**, 464 (2013).

26. Okubo, T., Chung, S. & Kawamura, H. Multiple-q states and the skyrmion lattice of the triangular-lattice heisenberg antiferromagnet under magnetic fields. *Phys. Rev. Lett.* **108**, 017206 (2012).

27. Leonov, A. O. & Mostovoy, M. Multiply periodic states and isolated skyrmions in an anisotropic frustrated magnet. *Nat. Commun.* **6**, 8275 (2015).

28. Hayami, S., Lin, S.-Z. & Batista, C. D. Bubble and skyrmion crystals in frustrated magnets with easy-axis anisotropy. *Phys. Rev. B* **93**, 184413 (2016).

29. Lin, S.-Z. & Hayami, S. Ginzburg-Landau theory for skyrmions in inversion-symmetric magnets with competing interactions. *Phys. Rev. B* **93**, 064430 (2016).

30. Ozawa, R. et al. Vortex crystals with chiral stripes in itinerant magnets. *J. Phys. Soc. Jpn.* **85**, 103703 (2016).

31. Hayami, S., Ozawa, R. & Motome, Y. Effective bilinear-biquadratic model for noncoplanar ordering in itinerant magnets. *Phys. Rev. B* **95**, 224424 (2017).

32. Jung, M. H. et al. Suppression of p-f mixing and formation of a superzone gap in $CeSbNi_x$. *Phys. Rev. B* **62**, 13860–13863 (2000).

33. Maurya, A., Dhar, S. K., Thamizhavel, A. & Road, H. B. Superzone gap formation and low lying crystal electric field levels in $PrPd_2Ge_2$ single crystal. Preprint at http://arxiv.org/abs/1702.00220 (2018).

34. Park, T., Sidorov, V. A., Lee, H., Fisk, Z. & Thompson, J. D. Pressure-tuned first-order phase transition and accompanying resistivity anomaly in $Ce Zn_{1-\delta}Sb_2$. *Phys. Rev. B* **72**, 060410 (2005).

35. H, L. et al. Magnetic order and transport in the heavy-fermion system $CeCu_{6-x}Au_x$. *Eur. Phys. J. B* **5**, 447 (1998).

36. Böhmer, A. E., Hardy, F., Wang, L., Wolf, T., Schweiss, P. & Meingast, C. Superconductivity-induced re-entrance of the orthorhombic distortion in $Ba_{1-x}K_xFe_2As_2$. *Nat. Commun.* **6**, 7911 (2015).

37. Park, J., Sakai, H., Erten, O., Mackenzie, A. P. & Hicks, C. W. Effect of applied orthorhombic lattice distortion on the antiferromagnetic phase of $CeAuSb_2$. *Phys. Rev. B* **97**, 024411 (2018).

38. Ishida, K. et al. Novel electronic nematicity in heavily hole-doped iron pnictide superconductors. *Proc. Natl. Acad. Sci. USA* **117**, 6424 (2020).

39. Deguchi, K. et al. Quantum critical state in a magnetic quasicrystal. *Nat. Mater.* **11**, 1013–1016 (2012).

40. Kamiya, K. et al. Discovery of superconductivity in quasicrystal. *Nat. Commun.* **9**, 154 (2018).

41. Schmiedeshoff, G. M. et al. Versatile and compact capacitive dilatometer. *Rev. Sci. Instrum.* **77**, 123907 (2006).

Acknowledgements

Author contributions

S.S. and P.F.S.R. conceived the project. P.F.S.R. synthesized the single crystals. S.M.T. performed thermal expansion measurement. S.S. performed electrical resistivity measurement. F.R. and E.D.B. provided support for the experimental setup. S.H., Y.S., and S.-Z.L. performed analytical calculations and simulations. S.S., S.-Z.L., J.D.T., and P.F.S.R. wrote the paper with input from all authors. All authors participated in the discussion of the results and their interpretation.

Competing interests

The authors declare no competing interests.

Additional information

Supplementary information The online version contains supplementary material available at https://doi.org/10.1038/s42005-021-00558-8.

Correspondence and requests for materials should be addressed to S.S. or P.F.S.R.

Reprints and permission information is available at http://www.nature.com/reprints

Publisher's note Springer Nature remains neutral with regard to jurisdictional claims in published maps and institutional affiliations.